International Journal of
Geo-Information

MDPI

Article

Integrating a Three-Level GIS Framework and a Graph Model to Track, Represent, and Analyze the Dynamic Activities of Tidal Flats

Chao Xu and Weibo Liu *

Department of Geosciences, Florida Atlantic University, Boca Raton, FL 33431, USA; cxu2018@fau.edu
* Correspondence: liuw@fau.edu; Tel.: +1-561-297-4965

Abstract: Tidal flats (non-vegetated area) are soft-sediment habitats that are alternately submerged and exposed to the air by changeable tidal levels. The tidal flat dynamics research mainly utilizes the cell-level comparisons between the consecutive snapshots, but the in-depth study requires more detailed information of the dynamic activities. To better track, represent, and analyze tidal flats' dynamic activities, this study proposes an integrated approach of a three-level Geographic Information Science (GIS) framework and a graph model. In the three-level GIS framework, the adjacent cells are assembled as the objects, and the objects on different time steps are linked as lifecycles by tracking the predecessor–successor relationships. Furthermore, eleven events are defined to describe the dynamic activities throughout the lifecycles. The graph model provides a better way to represent the lifecycles, and graph operators are utilized to facilitate the event analysis. The integrated approach is applied to tidal flats' dynamic activities in the southwest tip of Florida Peninsula from 1984 to 2018. The results suggest that the integrated approach provides an effective way to track, represent, and analyze the dynamic activities of tidal flats, and it offers a novel perspective to examine other dynamic geographic phenomena with large spatiotemporal scales.

Keywords: three-level GIS framework; graph model; dynamic activities; lifecycle; tidal flats

Citation: Xu, C.; Liu, W. Integrating a Three-Level GIS Framework and a Graph Model to Track, Represent, and Analyze the Dynamic Activities of Tidal Flats. *ISPRS Int. J. Geo-Inf.* **2021**, *10*, 61. https://doi.org/10.3390/ijgi10020061

Academic Editors: Wolfgang Kainz, Cristina Ponte Lira and Rita González-Villanueva

Received: 8 December 2020
Accepted: 28 January 2021
Published: 1 February 2021

1. Introduction

The study of dynamic geographic phenomena is a challenging topic in Geographic Information Science (GIS). In this topic, the core issue is the spatiotemporal characteristics of the study subjects, and the prerequisite is to identify and delineate the study subjects from the source data. Compared with the delineation, a more critical problem is how to track better, represent, and analyze the dynamic activities from the delineated results, which can help obtain the relevant information to fully describe the spatiotemporal characteristics of dynamic geographic phenomena and explain the reasons behind them.

In the GIS community, modeling the dynamic activities of geographic phenomena has been discussed, developed, and refined during the past several decades. As summarized by Worboys (2005) [1], this procedure can be divided into three stages: (1) the temporal snapshots, (2) the object changes, and (3) the events and action. As the delineated results can represent the static state of the dynamic geographic phenomena at one single moment, the first stage makes it possible to find the temporal sequences of objects, their attributes, and relationships by associating the states at different moments along the time sequence. For instance, Armstrong (1988) [2] proposes the snapshot view, which allows the query for the temporal information of a single object and all items associated with a given time. In addition, Worboys (2005) [1] points out that the time domain should allow interpolation between measurements in case of the continuous movements. However, the researchers often feel frustrated when considering the changes, because the first stage focuses on the temporal sequences of snapshots only [3]. In response to the new challenges, the second stage shifts the focus to the changes retrieved from the series of temporal snapshots. Hornsby and Egenhofer (2000) [4] emphasize that the change identification should be based on the comparison between the subsequent snapshots. As one of the earliest attempts, Peuquet and Duan (1995) [5] propose a data model that explicitly represents the changes based on the temporal comparisons in sequence. On the other hand, Claramunt and Thériault (1995) [6] propose a temporal framework focused on the geographic entities' topological changes, which provides a novel perspective to examine the complex evolution of dynamic geographic phenomena. However, the second stage's changes can only contribute to the preliminary representation and analysis for the dynamic geographic phenomena, and therefore, the third stage is developed in response to the new challenges. As a breakthrough, Yuan (2001) [7] systematically organizes a framework in which a temporal sequence of states forms a process, and a temporal aggregation of the processes makes an event.

In the third stage, Worboys (2005) [1] highlights "the *continuants* that endure through time" and "the *occurrents* that happen or occur and are then gone". This perception further deepens and expands the concept of objects in the second stage, and it yields the event-based perspective, which provides a possible way to better model the dynamic geographic phenomena. The objects can be tracked as lifecycles through which the dynamic activities can be observed [8]. McIntosh and Yuan (2005) [9] propose a four-level framework (zone, sequence, process, and event), which facilities the spatiotemporal query and analysis for the distributed dynamic geographic phenomena, and a case study of rainstorms is implemented. In addition, the following studies of marine dunes [10], ocean eddies [11], convective storms [12], urban heat islands [13], and Land Use and Land Cover (LULC) [14] have also endorsed the good performance of the event-based model. However, due to the data availability and computing performance, the previous studies often face the challenges of domain selection and spatiotemporal scale limitation. The in-depth study of event-based model is expected to eliminate these shortcomings with the aid of high-performance computing.

As a following issue, a good representation strategy could not only contribute to the visualization of the lifecycles but also facilitate the further analysis of the dynamic activities. More recently, the graph theory has been applied to GIS studies, which provides a possible solution to better represent the lifecycles. Thibaud et al. (2013) [10] utilizes a spatiotemporal graph model, in which "the graph edges are associated with the concepts of spatial relations and filiation relations". Cheung et al. (2015) [15] suggests that a sequence of snapshots at particular time steps can be threaded together into a single spatiotemporal graph, which provides an enhanced way to visualize the evolutionary trajectories over time. Furthermore, Wu et al. (2016) [16] proves that the graph theory can demonstrate a concise and intuitionistic way to capture and represent the storm-induced coastal changes. As the lifecycles are represented as graphs, the dynamic activities have great potential to get further analyzed with graph operators and algorithms. Previous studies mainly concentrate on the representation and visualization of dynamic geographic phenomena via the graph model, so it needs further study on how to adapt the graph algorithms to fully explore the dynamic activities in different domains.

In this study, we select the tidal flat as the subject of research. It is the coastal sediment that is alternately and periodically submerged in water and exposed to the air by the changeable tidal levels. As the land–sea interactions take place, the temperature, salinity, and acidity in the tidal flat region become variable [17]. A unique type of wetland ecosystem is the product under the above physical and chemical conditions, which is the homeland of shorebird [18], fungus [19], plankton [20], coastal fish [21], and so on. Aside from its contribution to biodiversity, the tidal flat also plays an important role in carbon preservation and global warming prevention [22–26]. In addition, the tidal flat has economic benefits. The unvegetated tidal flat all over the world contributes a total of $2.44 trillion USD per year as of the value in the year 2011 [27]. Hence, the dynamic activities of tidal flats have attracted the attention of researchers from different backgrounds.

It is essential to clarify the scope of the tidal flat region in this study because it can be defined in two ways. In a broad sense, the tidal flat region includes the bare intertidal flats, as well as the vegetated flats covered by salt marshes, mangroves, and seagrasses [28,29]. In a narrow sense, the tidal flat region only includes the unvegetated intertidal flats [30,31]. This study explicitly aims at the narrow sense of tidal flats (Figure 1).

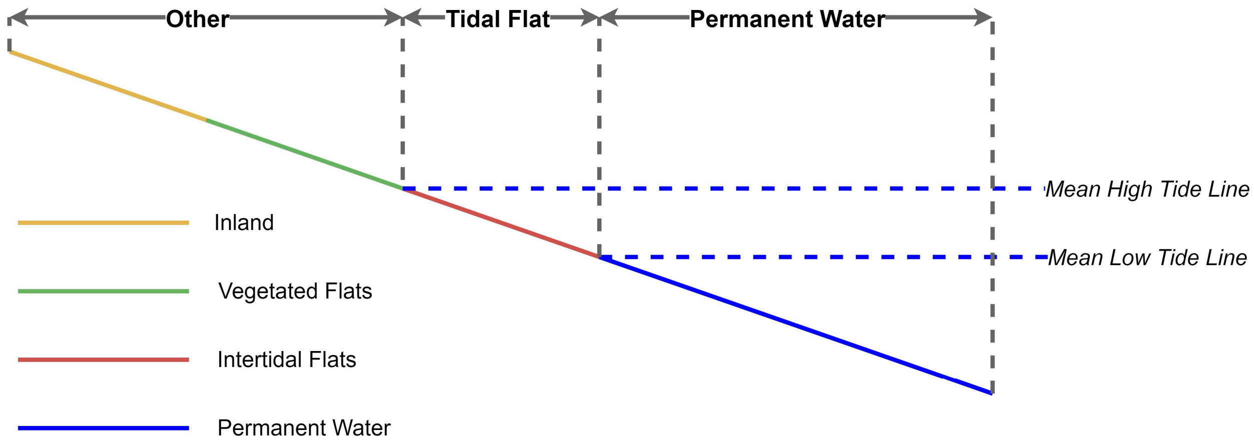

Figure 1. An illustration of the tidal flat region used in this study.

Following the existed theoretical basis, it is expected to propose a novel approach that facilitates the acquisition and summarization for the spatiotemporal characteristics of tidal flat dynamic activities. More specifically, the goal of this study is to integrate a three-level GIS framework and graph model. The three levels are as follows: (1) the cell level, which is the satellite image pixel of the tidal flat; (2) the object level, which is the set of contiguous tidal flat cells with a specific state at a specific moment; and (3) the lifecycle level, which is the set of tidal flat objects at different time steps linked as a chain based on the relative position relationships. In addition, different events to depict the dynamic activities can be derived from the lifecycle level. Therefore, this three-level GIS framework should be capable of tidal flat lifecycle tracking, which is the foundation of events capture. On the other hand, the graph model can convert the spatiotemporal information in the lifecycle level to the directed graphs, and its derivative spatiotemporal database offers the storage and query features for the morphologic attributes of the tidal flats throughout each individual lifecycle. Consequently, the graph can provide an enhanced way to represent the lifecycles and analyze the dynamic activities of tidal flats.

A case study is applied to the tidal flats in the southwest tip of the Florida peninsula from 1984 to 2018. Owing to the development of high-performance cloud computing in recent years, it has become feasible to access, process, and analyze geospatial big data, and therefore, our integrated approach can be applied to the larger spatiotemporal scales. With the available big datasets, the machine learning algorithms are widely used in cloud computing platforms. The random forest (RF) machine learning algorithm is used to delineate the cell level tidal flat information in this study.

2. Methods

2.1. Tidal Flat Cell Delineation

To study the spatiotemporal characteristics, it is essential to delineate the cells of the dynamic phenomena from the satellite data [11]. As different types of LULC have different spectral characteristics, the remote sensing-derived spectral indices are commonly used for water body identification, which is the prerequisite for tidal flat cell delineation. These indices include the Normalized Difference Water Index (NDWI) [32], Land Surface Water Index (LSWI) [33], Modified Normalized Difference Water Index (MNDWI) [34], Automated Water Extraction Index (AWEI) [35], and so on.

Based on water body identification results, many efforts have been spent on delineating tidal flats from the satellite images. The conventional methods include linear regression [36], Gaussian function [37], Otsu thresholding [38,39], and frequency thresholding [29,40,41]. Compared with the above conventional methods, the RF could classify the cells with respect to multiple indices and their statistical distributions and provide higher robustness [42]. To date, the RF is widely used in LULC classification issues, such as cropland [43,44], woody vegetation [45], human settlement [46,47], coastal lands [48], and so on. For tidal flat cell delineation, several methods have been developed based on the RF. Zhang et al. (2019)'s RF-based method [28] used MNDWI, Normalized Difference Vegetation Index (NDVI) [49], LSWI, Enhanced Vegetation Index (EVI) [50], Modified Soil-Adjusted Vegetation Index (MSAVI) [51], and Soil Brightness [52]. Their methods extract both the intertidal flats and supratidal vegetated flats, but we focus on the unvegetated intertidal zone. Following Murray et al. (2019) [31], the indices used in this study include AWEI, NDWI, MNDWI, and NDVI. The four indices are expressed as Equations (1)–(4):

$$AWEI = \rho_{blue} + 2.5 \times \rho_{green} - 1.5 \times (\rho_{nir} + \rho_{swir1}) - 0.25 \times \rho_{swir2} \tag{1}$$

$$NDWI = \frac{\rho_{green} - \rho_{nir}}{\rho_{green} + \rho_{nir}} \tag{2}$$

$$MNDWI = \frac{\rho_{green} - \rho_{swir1}}{\rho_{green} + \rho_{swir1}} \tag{3}$$

$$NDVI = \frac{\rho_{nir} - \rho_{red}}{\rho_{nir} + \rho_{red}} \tag{4}$$

where ρ_{blue}, ρ_{green}, ρ_{red}, ρ_{nir}, ρ_{swir1}, and ρ_{swir2} are the surface reflectance values of the corresponding bands of the Landsat images. In addition to the above indices, the Landsat near-infrared band (NIR) and Landsat short-wave infrared (SWIR) band are also considered.

The Landsat images are categorized as stacks consisting of all images acquired within each year. For any cell with 30 meters' spatial resolution, we can get the results by computing AWEI, NDWI, and MNDWI from all cells at the same location on different images within the same stack. To get the spectral change pattern in a stack, we also compute the maximum, minimum, median, standard deviation, the 10th, 25th, 50th, 75th, and 90th percentiles, and the means of all inputs in the specified percentile ranges (0–10, 10–25, 10–90, 25–50, 25–75, 50–75, 75–90, and 90–100). However, for NDVI, NIR, and SWIR, we only calculate the means of interval between the 10th and 90th percentiles. At this point, there are 54 variables for each cell.

In addition, another two variables are used. (1) The first is the ETOPO1 Global Relief Model, which is developed by the National Oceanic and Atmospheric Administration (NOAA) of the US. It is a global relief model of the Earth's surface, which integrates land topography and ocean bathymetry [53]. (2) The second is the global surface water occurrence data. This dataset has generated the location and temporal distribution of surface water, as well as the statistics on the extent and change of these water surfaces with 30 meters' spatial resolution based on a total of 3,066,102 tiles of Landsat 5, 7, and 8 images, which were acquired between 16 March 1984 and 10 October 2015 [54]. These two variables combining with the 54 statistical results for each cell form 56 predictor variables. A pre-computed and pre-classified (tidal flat, permanent water, and other) sample point dataset is used as a training dataset for the RF machine learning algorithm.

After the classification and post-processing, we can get the binary images, in which the cells with the value of 1 correspond to the tidal flats and the cells with the value of 0 correspond to the non-tidal flats. To validate the result, we use the validation dataset via random stratified sampling [31]. As the tidal flat cell delineation is accomplished, the foundation for tidal flat object level has been laid.

2.2. Tidal Flat Object Delineation

In the two-dimensional space, one cell may have up to eight neighboring cells (up, down, left, right, upper-left, upper-right, lower-left, and lower-right) [55]. For the tidal flat cells satisfying this eight-neighboring definition, the component-labeling algorithm [56] can assemble them as a contiguous patch, which is a tidal flat object in the context of this study. In addition, we can define a threshold to discard those too small tidal flat objects that may potentially add unnecessary complexity to the further analysis [12]. The threshold selection should be with respect to the spatial resolution and the size of the study area.

The objects generated from different domains, such as ocean eddies [11], convective storms [12], and urban heat islands [13], can be tracked and linked as time-series chains based on the relative positions between two objects on different time steps. These previous studies prove that the object modeling is the foundation of the lifecycle tracking. Specific to this study, the object delineation plays as the foundation of capturing the morphological dynamics of tidal flats, which is invisible in the conventional (cell-level) assessment.

2.3. Tidal Flat Lifecycle Tracking

For the tidal flat lifecycle tracking, the strategy should always be determined by the characteristics of the specific subject of research [11]. For the tidal flat lifecycle tracking, the overlapping method is realized, which finds the overlapping region between the two objects at the two adjacent time steps, considering the area ratios of the overlapping region to the two objects; then, it determines whether the two objects can be associated or not. In our study, for a pair of tidal flat objects, α is the object at the previous time step, β is the object at the current time step, and γ is the overlapping region between α and β. The overlapping ratio, R, is formularized as:

$$R = \frac{A_\gamma}{A_\alpha} + \frac{A_\gamma}{A_\beta} \tag{5}$$

where A_α, A_β, and A_γ are the areas of α, β, and γ, respectively. The value of R should not be less than 0, which corresponds to no overlapping case, and it should not be greater than 2, which corresponds to the exactly overlapping case. A threshold is defined to determine whether the two objects can get linked or not. As α and β are linked, a predecessor–successor relationship is established, in which α is the predecessor and β is the successor. The predecessor–successor relationships links the tidal flat objects between consecutive images, which refers to the lifecycle in this study.

For the objects within the derived lifecycle, the numbers of their predecessors and successors may vary, and the areas of each pair of predecessor and successor may be different. To categorize the dynamic activities of tidal flats, we firstly define six events according to the numbers of the predecessors and successors (Figure 2). In addition, we further define five events based on the area comparison between the predecessor and successor (Figure 3).

The object(s) on the first, second, and third time step are represented as A(s) (in red), B(s) (in blue), and C (in yellow), respectively. The solid line means the actual-existed object, and the dashed line means the pseudo-object (Figure 2). The six events according to the numbers of predecessors and successors include:

- *Appearance*: when the object B has no predecessors (Figure 2a);
- *Disappearance*: when the object A has no successors (Figure 2b);
- *Merger*: when the object B has two or more predecessors (A_1, A_2 . . . , A_n) (Figure 2c);
- *Ssplitting*: when the object A has two or more successors (B_1, B_2 . . . , B_n) (Figure 2d);
- *Continuation*: when the predecessor A has exactly one successor B, and the successor B has exactly one predecessor A (Figure 2e); and
- *Recovery*: when a group of linked objects starts with a splitting and end with a merger (Figure 2f).

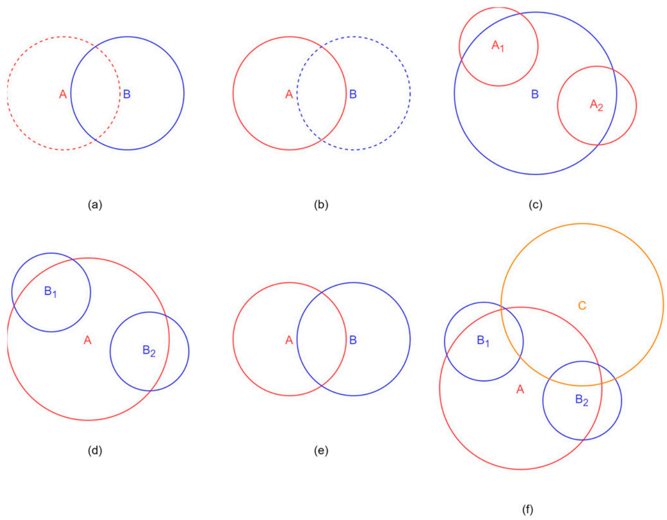

Figure 2. The illustration of the six events based on the numbers of predecessors and successors: (**a**) appearance; (**b**) disappearance; (**c**) merger; (**d**) splitting; (**e**) continuation; and (**f**) recovery.

The object(s) on the first time step and the second time step, the overlapping region(s), and the largest overlapping region are represented as A(s), B(s), C(s), and C_{max}, respectively. The five events based on the area comparison between the predecessor and successor include:

- *Expansion*: in case of *continuation*, the B's area is greater than or equal to 110% of the A's area (Figure 3a);
- *Stability*: in case of *continuation*, the ratio of the B's area to the A's area is between 90% and 110% (Figure 3b);
- *Contraction*: in case of *continuation*, the B's area is smaller than or equal to 90% of the A's area (Figure 3c);
- *Annexation*: in case of *merger*, multiple A(s) $\{A_1, A_2 \ldots, A_n\}$ and the B share multiple C(s) $\{C_1, C_2 \ldots, C_n\}$. If the area of C_{max} is greater than or equal to 65% of the B's area, it is an *annexation* (Figure 3d); and
- *Separation*: in case of *splitting*, the A and multiple B(s) $\{B_1, B_2 \ldots, B_n\}$ share multiple C(s) $\{C_1, C_2 \ldots, C_n\}$. If the area of C_{max} is greater than or equal to 50.01% of the A's area, it is a *separation* (Figure 3e).

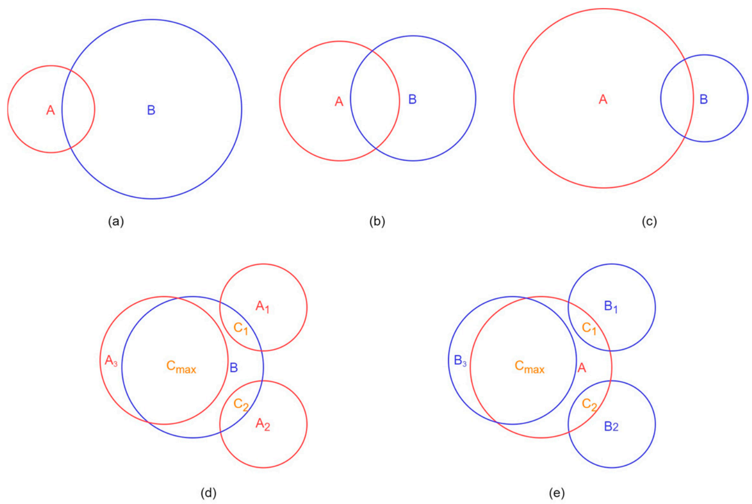

Figure 3. The illustration of the five events based on the area comparison between the predecessor and successor: (**a**) expansion; (**b**) stability; (**c**) contraction; (**d**) annexation; and (**e**) separation.

To demonstrate the tidal flat lifecycle tracking procedure, three consecutive snapshots taken at different time steps (t_1, t_2, and t_3) are provided as an example (Figure 4), which form a three-dimensional space (X, Y, T). There are a total of three tidal flat objects (A_1, C_1, and E_1) at t_1, six tidal flat objects (A_2, B_1, C_2, D_1, E_2, and E_3) at t_2, and four tidal flat objects (B_2, B_3, C_3, and E_4) at t_3. For better reference, the locations of some tidal flat objects are projected on the adjacent snapshots, which are marked with undertint colors and dashed lines such as A_1' of A_1.

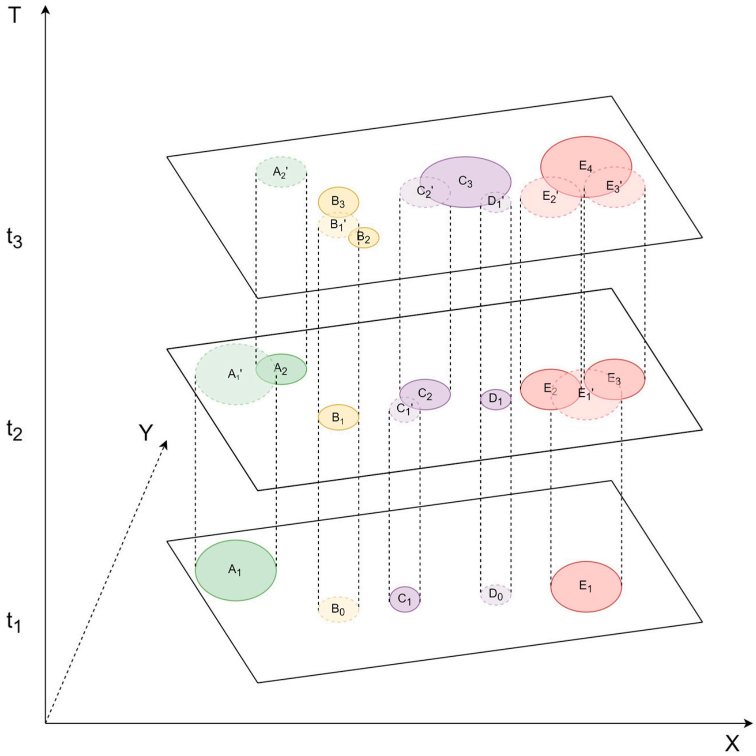

Figure 4. A tidal flat lifecycle tracking example.

As Figure 4 shows, A_1' is the projection of A_1 at t_2, which shares sufficient overlapping area with A_2; therefore, the predecessor—successor relationship is established, where A_1 is the predecessor and A_2 is the successor, and a *continuation* happens to them. The other predecessor–successor relationships in this figure are all established in the same way, which contribute a total of four tidal flat lifecycles. All other types of events based on the numbers of predecessors and successors are also visible in this figure: A_2' is the projection of A_2 at t_3, and we can find nothing overlaps with it, so A_2 has no successors and a *disappearance* occurs. Similarly, B_0 is the projection of B_1 at t_1, and we can find nothing overlaps with it, so B_1 has no predecessors and an *appearance* occurs. On the other hand, B_1' is the projection of B_1 at t_3. It overlaps with B_2 and B_3, which indicates that B_1 has two successors, and a *splitting* comes out. C_2' and D_1' are the projections of C_2 and D_1 at t_3, and both overlap with C_3. It means C_3 has two predecessors and a *merger* happens. In the same way, we could find E_2 and E_3 are the successors of E_1, and they are also the predecessors of E_4. These four objects form a *recovery*.

2.4. Graph Representation and Analysis for Tidal Flat Lifecycles

In graph theory, the graph is defined as "a representation of a set of points (the nodes) and of how they are joined up (the edges), and any metrical properties are irrelevant" [57]. Since the graph is a concise way to deliver the information, it has been widely used in GIS to represent the evolutionary procedures of dynamic geographic phenomena. Moreover, the graph operators provide an effective way to capture the events automatically and exhaustively from a large amount of tidal flat lifecycles, which also highlights that the object and lifecycle levels could provide more diversified dynamic information than the cell level.

In this study, the tidal flat objects are represented by their centroids, and the predecessor–successor relationships are represented by the directed edges from the predecessors to the successors. The centroids form the node set V(G) and the directed edges form the set E(G), which constitute the directed graph G in two-dimensional space (X, Y). To demonstrate how the graph works in this study, the information of Figure 4 is derived as graphs and drawn in Figure 5. In this figure, it is easy to read the predecessor–successor relationships and the corresponding six events based on the numbers of predecessors and successors including *appearance*, *disappearance*, *splitting*, *merger*, *continuation*, and *recovery*.

As the graphs are derived, the information of each individual tidal flat lifecycle is collected, organized, and stored in a spatiotemporal database simultaneously (Figure 6). This database can help us better understand and query the morphological changes between the adjacent tidal flat objects, which are invisible in Figure 5, because tidal flat objects are represented by their centroids as the nodes. Especially, the five events defined in Section 2.3 are determined by the area comparison between the predecessor and successor, and this spatiotemporal database can help us capture these events. Moreover, for the six events based on the number of predecessors and successors, we introduce two graph operators to assist the analysis for tidal flat dynamic activities.

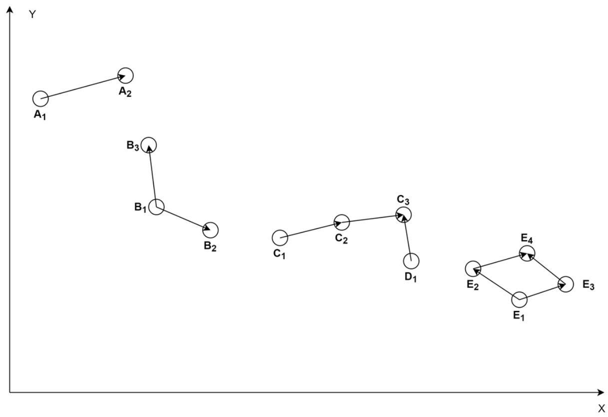

Figure 5. The four lifecycle graphs derived from Figure 4.

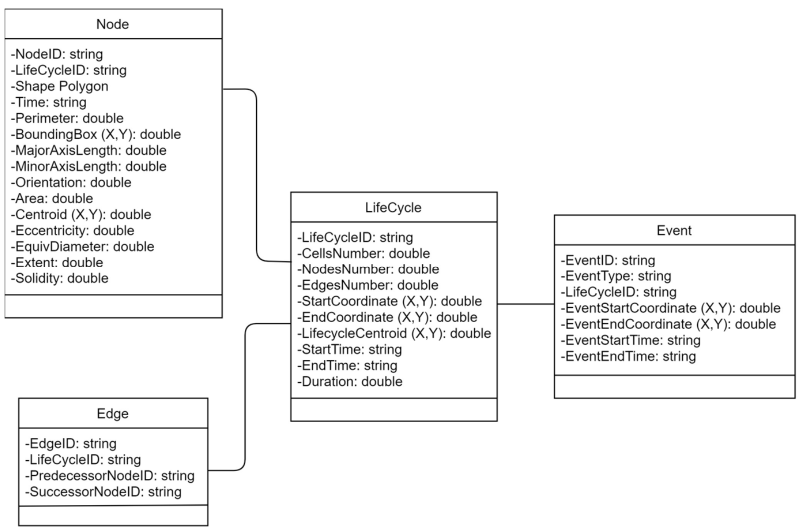

Figure 6. The structure of the spatiotemporal database.

2.4.1. Use Degree to Identify Five Events

For any node in a graph, its degree is defined as the number of edges connected to this node. For a directed graph, the degree of the node is further divided into indegree and outdegree. The indegree is defined as the number of arrows ending at this node, and the outdegree is defined as the number of arrows starting from this node [57]. In the context of this study, for any object, the indegree of its corresponding node equals the number of its predecessors, and the outdegree of its corresponding node equals the number of its successors.

Based on this perception, the five events based on the numbers of predecessors and successors correspond to the following cases:

- *Appearance*: when the node's indegree is 0;
- *Disappearance*: when the node's outdegree is 0;
- *Splitting*: when the node's outdegree is greater than or equal to 2;
- *Merger*: when the node's indegree is greater than or equal to 2; and
- *Continuation*: when the successor node's indegree is 1 and the predecessor node's outdegree is also 1.

2.4.2. Find Non-Cut Vertex to Identify the Event of Recovery

A node v of a graph G is a cut vertex if the removal of v increases the number of components of G [57]. Apparently, the starting and ending nodes, which correspond to *appearance* and *disappearance*, are not the cut vertices. For the tidal flat lifecycles, which do not include the event of *recovery*, the rest nodes must be cut vertices. On the other hand, according to the definition of *recovery*, there are at least two parallel paths that exist between (but do not include) the *splitting* and *merger* nodes, and the nodes on the parallel paths are not the cut vertices. Therefore, we can justify whether a tidal flat lifecycle includes the *recovery* event or not by calculating the number of non-cut vertices other than the starting and ending nodes. If the number equals to zero, the tidal flat lifecycle has no *recovery* event; if the number is positive, the tidal flat lifecycle must include at least one *recovery* event.

3. A Case Study

3.1. Data and Study Area

The following datasets are used in this case study: (1) Landsat TM (Thematic Mapper), ETM+ (Enhanced Thematic Mapper Plus), OLI (Operational Land Imager), and TIRS (Thermal Infrared Sensor) acquired by Landsat 4, 5, 7, and 8 during 1984 to 2018; (2) the ETOPO1 Global Relief Model; (3) the global surface water occurrence data; (4) the training point dataset; and (5) the validation point dataset. We use Google Earth Engine (GEE), a high-performance cloud computing platform, to access and process the above datasets and implement the RF machine learning algorithm. More than thirty years of geospatial datasets have been stored in the GEE virtual archives, which occupy over twenty petabytes of space and are updated and expanded daily. These large datasets can be instantly invoked and processed by the high-performance computing resources [58].

The case study area is the southwest tip of Florida peninsula, which belongs to the counties of Collier, Monroe, and Miami-Dade. This area is located within the coverage of the Landsat tiles of Path=15 Row=42, Path=15 Row=43, and Path=16 Row=42 (Figure 7). From 1984 to 2018, a total of 2906 tiles of Landsat 4, 5, 7, and 8 images in this area have been pre-processed to surface reflectance Tier 1, and all of them are used to delineate the tidal flat cells in this study. The annual distribution of available Landsat images is shown in Figure 8. In this figure, we categorize these images by year and get a total of 35 annual stacks from 1984 to 2018, which include 14 tiles of Landsat 4 (LT4) images, 1351 tiles of Landsat 5 (LT5) images, 1177 tiles of Landsat 7 (LE7) images, and 364 tiles of Landsat 8 (LC8) images.

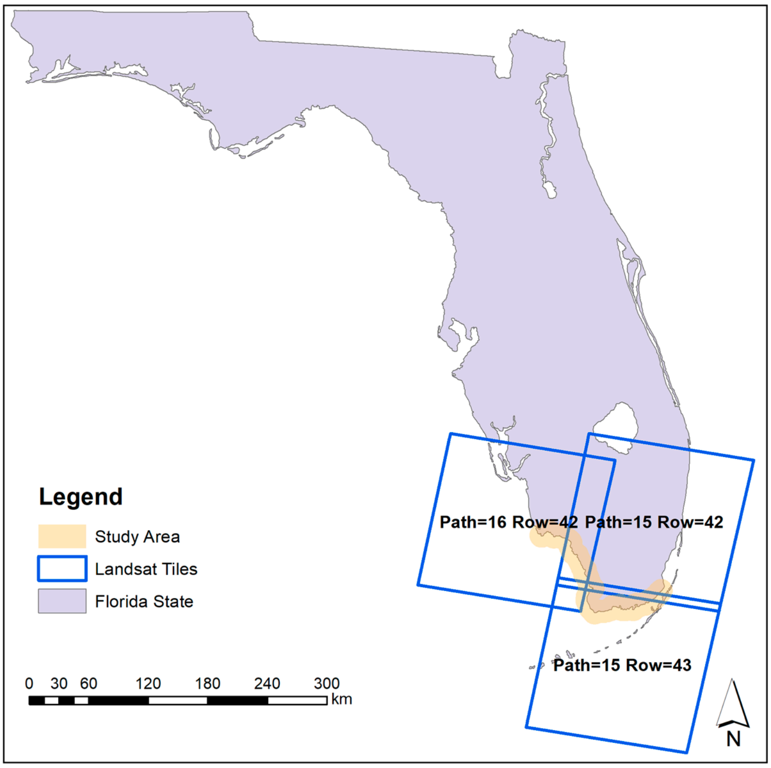

Figure 7. The case study area and the coverage of Landsat tiles.

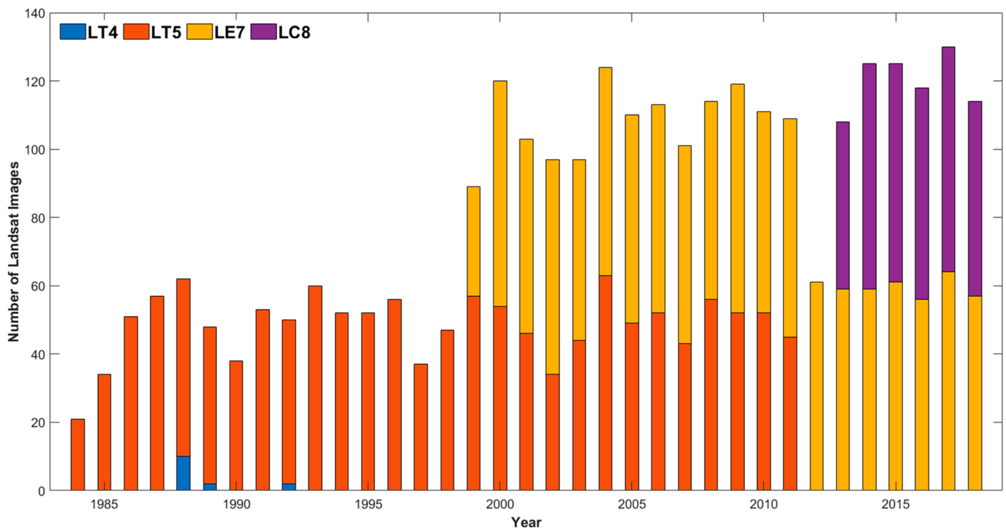

Figure 8. Annual distribution of available Landsat images.

A major part of this study area belongs to Everglades National Park. Geologically, the study area is divided into two subprovinces: the west coastal area belongs to the Ten Thousand Islands Subprovince, while the south coastal area belongs to the Southern Atlantic Coastal Strip Subprovince. The Ten Thousand Islands Subprovince is the transitional area between the Everglades and Gulf of Mexico, which consists of tidal flats, lagoons, uninhabited islands, mangrove forests, and highly productive estuaries. As the climate changes, the sea level fluctuates, while the sediment grows and recedes over time. Tidal flat is one of the products during this procedure, which plays an important role in protecting the inland areas from the hurricane-caused floods and breaking waves in the Gulf of Mexico. The Southern Atlantic Coastal Strip Subprovince consists of marine limestone, which is covered by thin sheets of quartz sand. The limestone stops water in the Everglades from flowing into the Atlantic Ocean. However, there is a marshy channel system across the limestone ridge (i.e., Taylor Slough), which drains the water in the Everglades into Florida Bay. As a result, the mud is deposited along the coast, and the tidal flat region is produced [59–62]. Hence, the study area has a sufficient tidal flat region, and it is regarded as an ideal place to implement the case study.

3.2. Implementation

As all available Landsat images are found and sorted by year, the case study can be implemented following Figure 9. The Landsat images acquired at the same time are mosaicked and clipped according to the study area's boundary. The clouds, cloud shadows, cirrus, and scan-line corrector (SLC)-off gaps are classified as bad-quality observations. To identify and eliminate them, the Function of mask (FMask) Algorithm is used in this study [63,64].

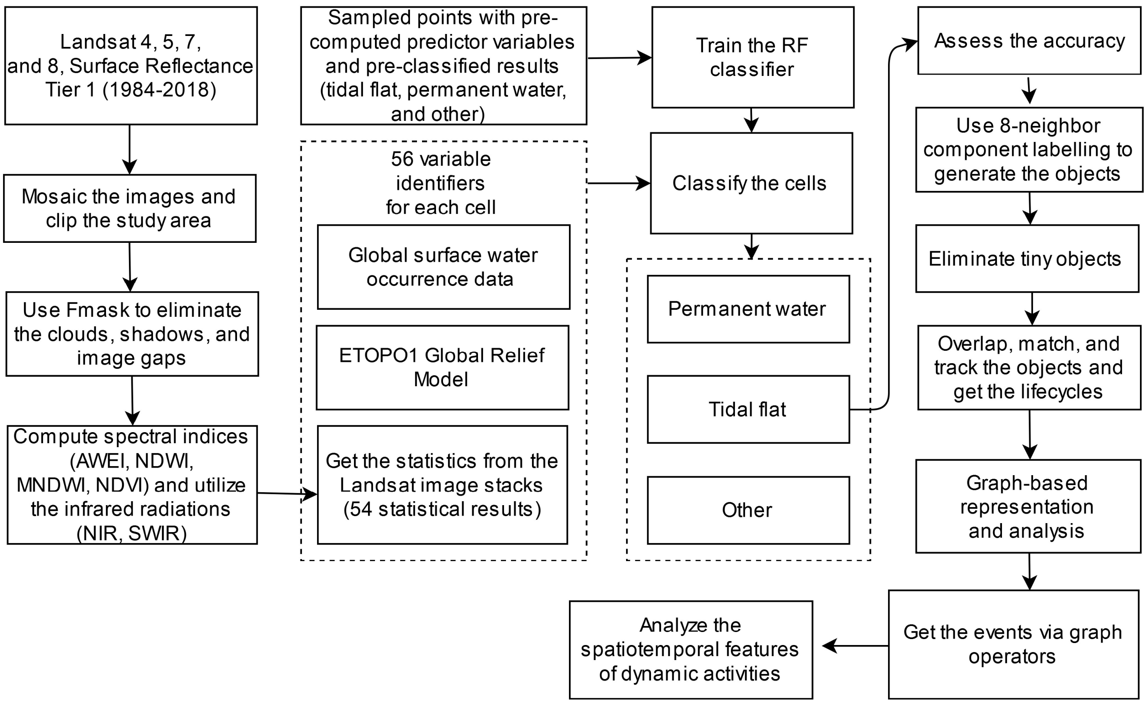

Figure 9. The general workflow of the study.

Next, we use the cells of the same location from all mosaicked–denoised images under the same annual stack to calculate the 56 predictor variables as described in Section 2.1. As the predictor variable calculation and the RF classifier training are finished, the RF classification could delineate the tidal flat cells and have an overall accuracy of 95.23%. In the end, every annual stack contributes one binary image. The following processes will be operated based on this tidal flat cell delineation result.

As shown in Figure 9, the following processes are tidal flat object assemblage, lifecycle tracking, the graph-based representation, and the spatiotemporal analysis of events. Proceeding with the work, a prototype system is developed via MATLAB. A threshold value of 3 is used to discard the tidal flat objects, which are smaller than three cells' coverage area (2700 m^2), and the value of 0.6 is used as the overlapping threshold (Equation (5)) to determine the predecessor–successor relationship.

Based on the implemental procedures as illustrated above, we get the graphs of tidal flat lifecycles, and the spatial, temporal, and morphologic attributes of tidal flats are stored in the database. The graph operators are used to analyze the generated graphs and get the spatiotemporal characteristics for each type of event. The results of this case study are shown and discussed in Section 3.3.

3.3. Results and Discussion

3.3.1. Characteristics of Tidal Flat Cells, Objects, and Lifecycles

As described in Section 3.2, we get a total of 35 binary images, which are the annual records of the tidal flat cells from 1984 to 2018. To demonstrate the delineation result, Figure 10 shows the annual tidal flat area from 1984 to 2018. As shown in the figure, the maximum record (262.5 km^2) happened in 1992, which is significantly greater than the mean annual area (129.39 km^2) and the second maximum record (173.1 km^2 in 2008). Hurricane Andrew (Category 5) may be used to explain the unusual record in 1992. According to Risi et al. (1995) [65], this hurricane created a substantial amount of sediment deposits along the shallow subtidal coastline in our study area.

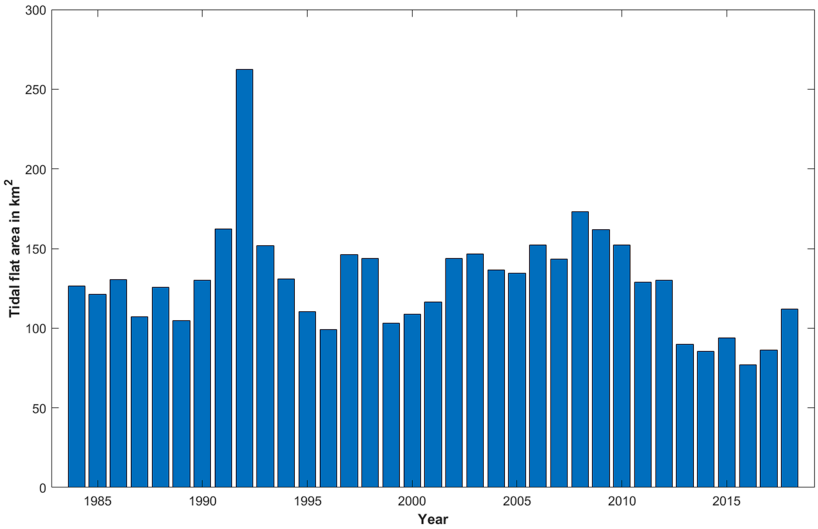

Figure 10. Annual distribution of the tidal flat area.

To better understand the spatial distribution of the delineated tidal flat cells, we aggregate the occurrences of tidal flat cells based on all 35 binary images (Figure 11). As shown, the tidal flat cells in different years are heavily overlapped, and they are mostly distributed in four regions: (A) the northwestern corner of the study area; (B) the middle portion of the west coast; (C) the turning point between the west coast and south coast; and (D) the eastern portion of the south coast. Region A belongs to Rookery Bay National Estuarine Research Reserve, which is one of the few remaining undisturbed mangrove estuary system in North America. This system plays an important role for the resuspension and transportation of sediments and contributes to an advantageous environment for tidal flat dynamic activities [66]. Similarly, region C is located around Cape Sable, in which a man-made canal project was carried out in 1922. This project has largely changed the hydrologic environment of the surrounding area. As a result, an active tidal flat region was produced around Sandy Key Basin, which is located off the coast of Cape Sable [67]. On the other hand, region B is located around the estuary of Shark River Slough, while region D is located around the estuary of Taylor Slough. These two rivers are the principal natural drainages that keep carrying the overland water and mud from the Everglades to the sea. Consequently, the tidal flat regions are intensive in the two places.

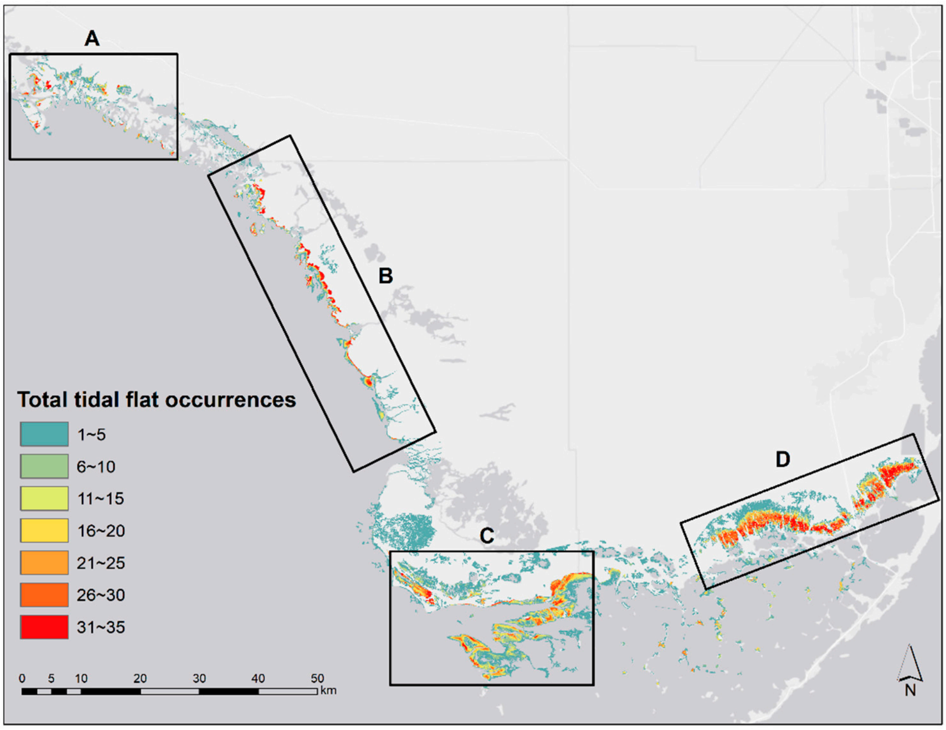

Figure 11. Spatial distributions of total tidal flat occurrences from 1984 to 2018. A, B, C, and D are four tidal flat intensive regions.

By comparing the 35 cell level maps, we can summarize the area changes of tidal flats in the above four regions and the rest of the region, as shown in Figure 12. Region A has the smallest annual average area among the four regions (8.22 km^2). The tidal flat area in this region periodically changes, as it reaches the peak every eleven years (1986, 1997, and 2008). The maximum area happened in 1997, which is 19.62 km^2, while the minimum area happened in 2016, which is only 1.87 km^2. Region B has the second smallest annual average area among the four regions (18.04 km^2). Its tidal flat area change also has regularity, as it reaches the peak every five to seven years (1986, 1991, 1997, 2002, 2008, and 2015). Similar to region A, the maximum tidal flat area of region B happened in 1997 (32.75 km^2), and the minimum tidal flat area (7.78 km^2) happened in 2017, which is only one year after that of region A. Region C has the second largest annual average area among the four regions (42.28 km^2). Although the regularity of the tidal flat area change is not significant, it is obvious that two peaks exist in 1989 and 2009, while there is a valley between these two peaks. The maximum area (72.61 km^2) happened in 2009, while the minimum area (8.84 km^2) happened in 1995. Region D has the largest annual average area among the four regions (51.43 km^2). Similar to region C, its tidal flat area change does not have significant regularity. The maximum area (100.3 km^2) happened in 1992, while the minimum area (14.96 km^2) happened in 1989. The annual average area of the tidal flat in the rest of the region is 9.42 km^2, which is only 7.3% of the annual average area of the tidal flat in the whole study area. It further proves that the tidal flat cells in the study area are mainly distributed in the four intensive regions.

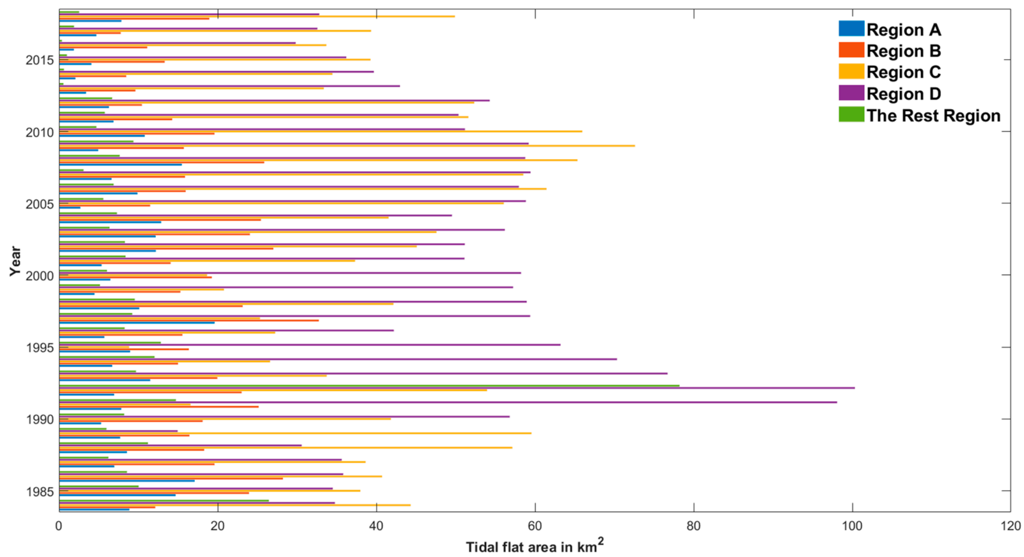

Figure 12. Annual distribution of tidal flat area by regions.

Based on the delineated tidal flat cells, a total of 3672 objects are assembled, and 962 tidal flat lifecycles are tracked from the study area. Every tidal flat lifecycle has a duration of at least one year. Figure 13 shows the duration distribution of these 962 tidal flat lifecycles and gives the mean duration of 2.8 years. As shown in the figure, a total of 476 tidal flat lifecycles have the duration of only one year, which are nearly half of the tracked tidal flat lifecycles. There are 863 tidal flat lifecycles that have 5 years or less duration, while only 99 tidal flat lifecycles live longer than five years. It is obvious that most tidal flat lifecycles have short durations.

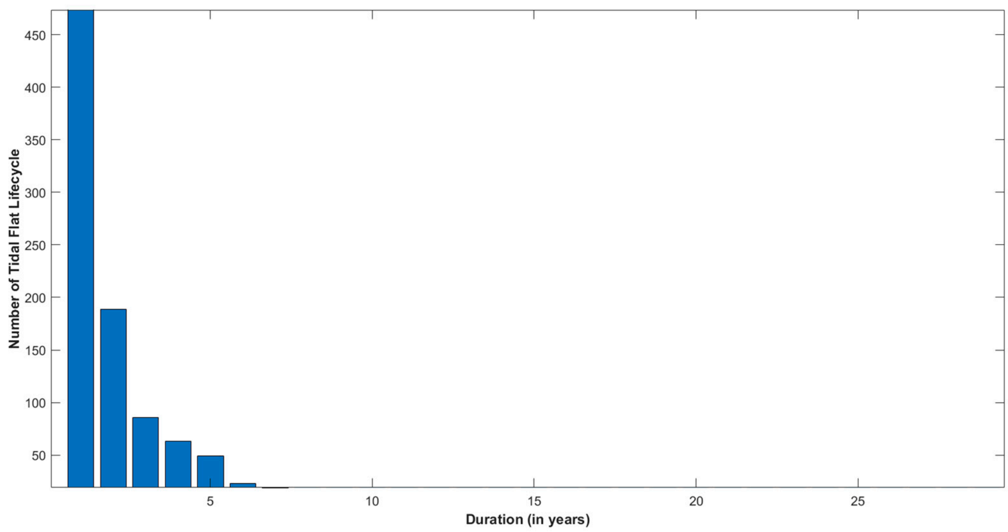

Figure 13. The duration distribution of the 962 tidal flat lifecycles.

To demonstrate the graph representation and analysis, we select the 178th tidal flat lifecycle as an example, and it is illustrated in Figure 14. This tidal flat lifecycle lasts six years (1984–1990) and includes a variety types of events, so it is considered as an ideal case to be analyzed. The location of this tidal flat lifecycle within the whole study area is shown in Figure 14a, which is in region D. As described in Figure 6, the starting and ending coordinates of each tidal flat lifecycle are stored in the spatiotemporal database, so we can easily query the location of any specified tidal flat lifecycle. Moreover, the locations of the tidal flat objects (represented by their centroids as the nodes) and the movement track (represented as the edges) within this lifecycle are shown in Figure 14b, which are also queried from the spatiotemporal database. The derived graph of Figure 14b is drawn in Figure 14c. Compared with Figure 14b, the derived graph in Figure 14c is a succinct version to illustrate the predecessor–successor relationships within the 178th tidal flat lifecycle. By calculating the indegree and outdegree of each object and querying the areas of each tidal flat object from the spatiotemporal database, we can easily summarize the event types existing in this lifecycle, which include *appearance*, *continuation* (*stability*), *splitting* (*separation*), *merger* (*annexation*), *recovery*, and *disappearance*. The corresponding event information is also stored in the database. This graph representation and analysis provide a straightforward way to examine the dynamic activities within an individual tidal flat lifecycle.

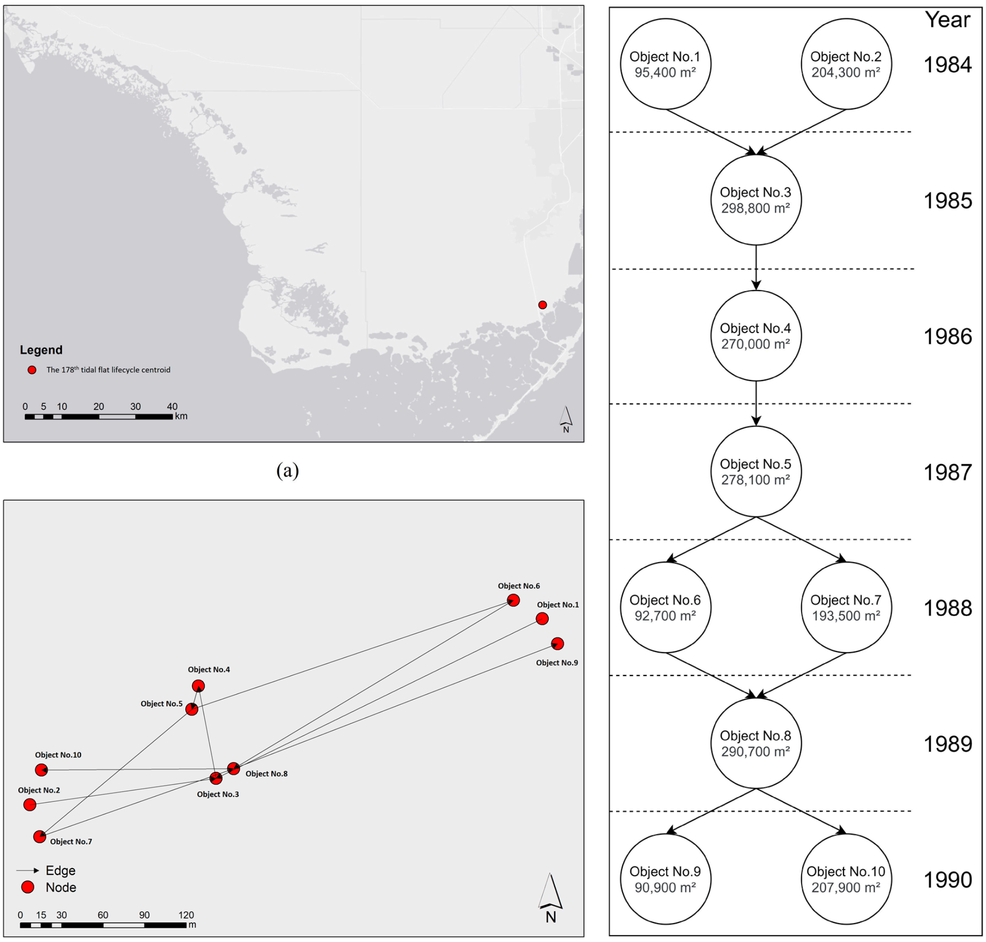

(c)

Figure 14. The lifecycle of the 178th tidal flat. (**a**) The centroid location of this lifecycle within the study area; (**b**) the actual movement of tidal flat objects within this lifecycle; and (**c**) the graph representation for this lifecycle.

As the first effort of the multi-level GIS framework on the issue of tidal flats, we examine the dynamic activities of tidal flats from a novel perspective. The temporal and spatial characteristics of tidal flat events are presented in the below sections. Since the cases of the *continuation* event are fully covered by three types of events based on the area comparison between the predecessor and successor (*contraction*, *stability*, and *expansion*), the below sections do not discuss the *continuation* event.

3.3.2. Temporal Characteristics of Tidal Flat Events

Annual numbers of *appearance*, *disappearance*, *splitting*, *merger*, and *recovery* are drawn in Figures 15 and 16. For better reference, the descriptive statistics derived from these two figures is shown in Table 1. As shown in Figure 15, the initial year (1984) in this case study has the historical maximum record of *appearance* (104). Apparently, it could be overestimated, because we do not have available data before 1984. Similarly, the tidal flat lifecycles that end in the final year (2018) may exist longer and disappear in the future years. To eliminate the interference, these two years' records of *appearance* and *disappearance* are both ignored in the statistics in Table 1.

From Figure 15, we can see that the annual occurrence of *appearance* is more stable than that of *disappearance*, and this preliminary observation can be verified in Table 1. As the smaller value of standard deviation implies higher stability, the event of *appearance* has the smaller standard deviation (σ = 7.76) than that of *disappearance* (σ = 9.93). In particular, there were 60 *disappearance* events in 2004 and 46 *disappearance* events in 2011, while the mean value of annual occurrence of *disappearance* is 27.51. We can conclude that the years of 2004 and 2011 have unusually higher occurrences of *disappearance*.

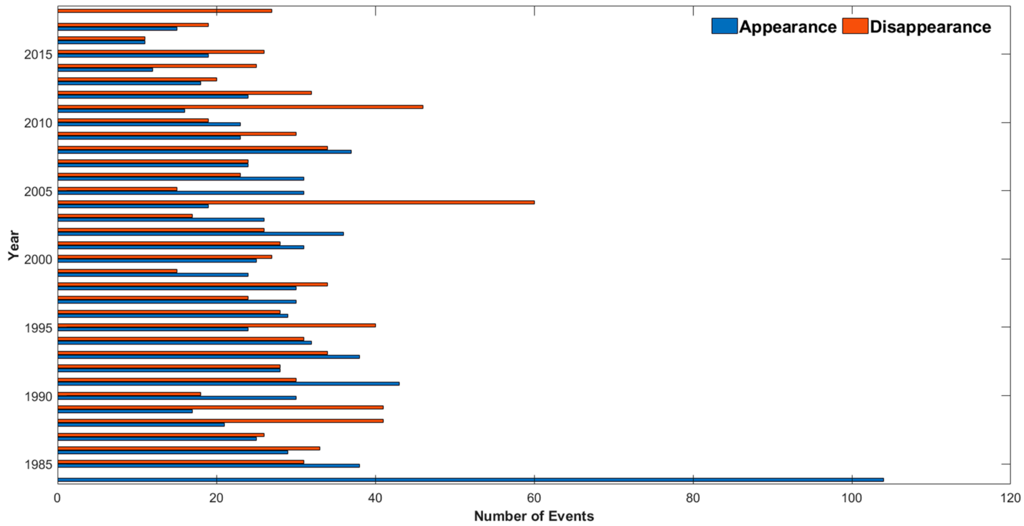

Figure 15. Annual distribution of the events of appearance and disappearance.

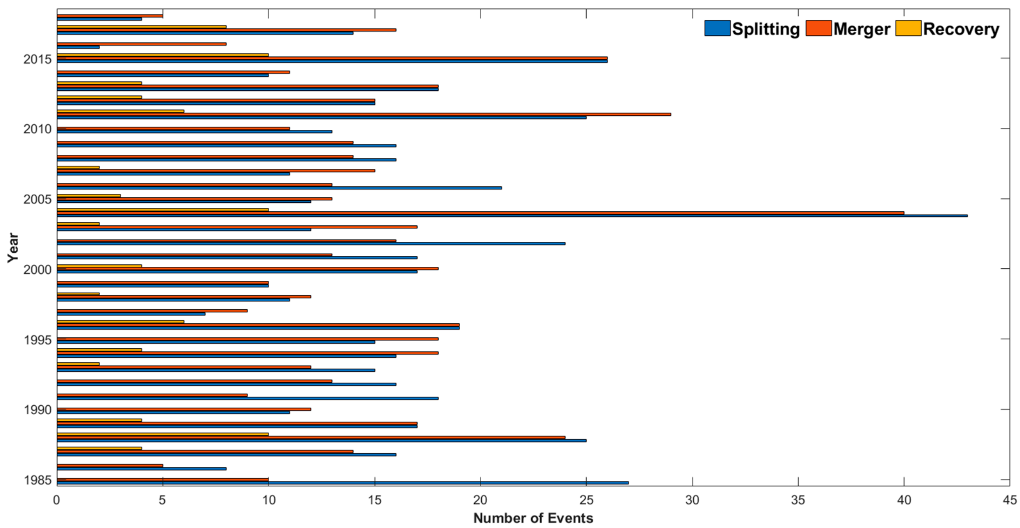

Figure 16. Annual distribution of the events of splitting, merger, and recovery.

In Table 1, we can also find the annual mean occurrences of *splitting*, *merger*, and *recovery* are 16.09, 15.12, and 2.50. Based on these mean values, we can find a total of five peaks with significantly higher event numbers than the corresponding mean values in Figure 16, which are in the years of 1988, 1996, 2004, 2011, and 2015. Aside from the peak in 2015, the other peaks imply a persistent and stable periodicity of about seven to eight years.

Table 1. The descriptive statistics of the events.

Event Type	Maximum	Minimum	Mean ($\bar{x}$)	Standard Deviation (σ)
Appearance	43 (1991)	11 (2016)	26.03	7.76
Disappearance	60 (2004)	11 (2016)	28.36	9.93
Splitting	43 (2004)	2 (2016)	16.09	7.59
Merger	40 (2004)	5 (2018)	15.12	6.82
Recovery	10 (1988, 2014, 2015)	0 (1985–1986, 1990–1992, 1995, 1997, 1999, 2001–2002, 2006, 2008–2010, 2014, 2016, 2018)	2.50	3.23
Contraction	44 (1987)	10 (2015)	29.32	8.68
Stability	42 (2004)	1 (2018)	17.44	7.48
Expansion	55 (1986)	5 (2016)	25.91	11.37
Annexation	10 (2003)	0 (2015)	3.91	2.53
Separation	24 (1985)	0 (2015-2018)	5.03	4.53

Note: The corresponding years are labeled in the round brackets.

The annual number and descriptive statistics for the events based on the area comparison between the predecessor and successor are shown in Figures 17 and 18, and Table 1. Figure 17 and Table 1 indicate that occurrences of *stability* ($\bar{x}$ = 17.44) are less than occurrences of *expansion* ($\bar{x}$ = 25.91) and *contraction* ($\bar{x}$ = 29.32), which further reveals that tidal flat objects tend to have significant area changes rather than keeping steady. However, there were 42 *stability* events in 2004 and 31 *stability* events in 2000, which are distinctly larger than the mean value of annual *stability* events. On the other hand, there were 34 *contraction* events and 28 *expansion* events in 2004, and there were 17 *contraction* events and 24 *expansion* events in 2000, which are less than the event numbers of *stability* in these two years. These comparisons demonstrate that the years of 2000 and 2004 have unusually more *stability* events.

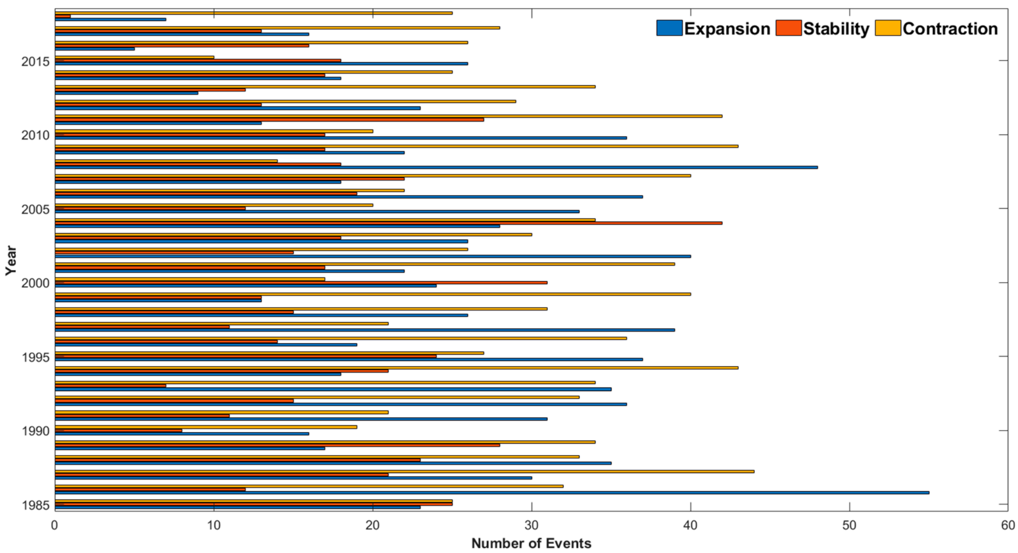

Figure 17. Annual distribution of the events of expansion, stability, and contraction.

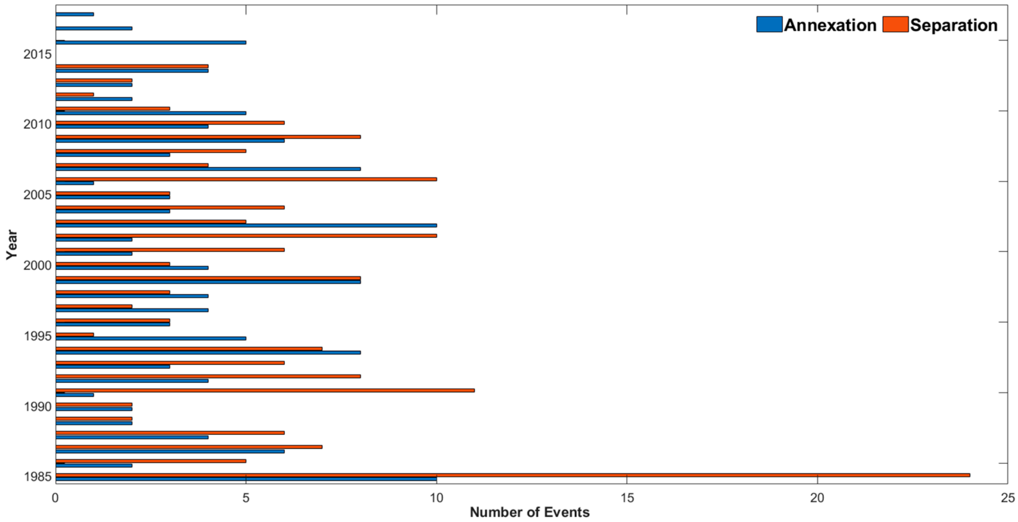

Figure 18. Annual distribution of the events of annexation and separation.

From Figure 18, we can find the periods when most *separation* events occurred are (1) from 1985 to 1993; (2) from 2001 to 2002; (3) from 2004 to 2006; and (4) from 2008 to 2010. A total of 125 *separation* events happened during these four periods, and the annual mean occurrence of the *separation* event during these four periods is 7.35, which is significantly larger than the overall annual mean of the event occurrence of *separation* ($\overline{x} = 5.03$). The periods when most of the *annexation* events occurred are (1) from 1994 to 2000; (2) the year of 2003; (3) the year of 2007; and (4) from 2011 to 2018. A total of 75 *annexation* events happened during these periods, and the annual mean of the event occurrence of *annexation* is 4.41, which is significantly larger than the overall annual mean of the event occurrence of *annexation* ($\overline{x} = 3.91$).

In addition to the above discoveries, another interesting finding is that the year of 2004 is a unique year. As suggested in Section 3.3.1, the hurricane activities may be the reason. There have been three hurricanes that affected the study area in that year, which are Hurricane Charley (Category 4), Hurricane Frances (Category 4), and Hurricane Ivan (Category 5) [68].

3.3.3. Spatial Characteristics of Tidal Flat Events

In addition to the temporal characteristics, the spatial characteristics of each type of event can be revealed by plotting the event occurrence places as points on the map. These event occurrence places are determined by the definitions of the specified types of events. In detail, the *disappearance*, *splitting*, and *separation* events are only defined by the number of successors. Therefore, each event must have exactly one predecessor node, which is regarded as the event occurrence place. However, for the rest event types, the terminal node is unique (i.e., the successor node of *appearance*, *continuation*, *contraction*, *stability*, *expansion*, *merger*, *annexation*, and the successor node of the *merger* is part of *recovery*). So, the occurrence places of these events are determined as the terminal node. For better visualization, a fishnet is created via ArcGIS to cover the whole study area, in which the size of each grid is 4 km^2. The number of event occurrences is counted for each grid, and the grid-based summary maps for all types of events are drawn in Figure 19. The preliminary observation of Figure 19 suggests that these event types can be classified as four categories according to their occurrences, in which the events of *appearance* (Figure 19a), *disappearance* (Figure 19b), *contraction* (Figure 19c), and *expansion* (Figure 19e) belong to the highest occurrence category, the events of *stability* (Figure 19d), *merger* (Figure 19f), and *splitting* (Figure 19h) belong to the second highest occurrence category, the events of *annexation* (Figure 19g) and *separation* (Figure 19i) belong to the third highest occurrence category, and the event of *recovery* (Figure 19j) belongs to the lowest occurrence category.

This finding is consistent with the comparison of the annual means ($\overline{x}$) in Table 1 and it is easy to understand, because the event of *annexation* is the special case of *merger*, event of *separation* is the special case of *splitting*, and the event of *recovery* is the special case of both *merger* and *splitting*.

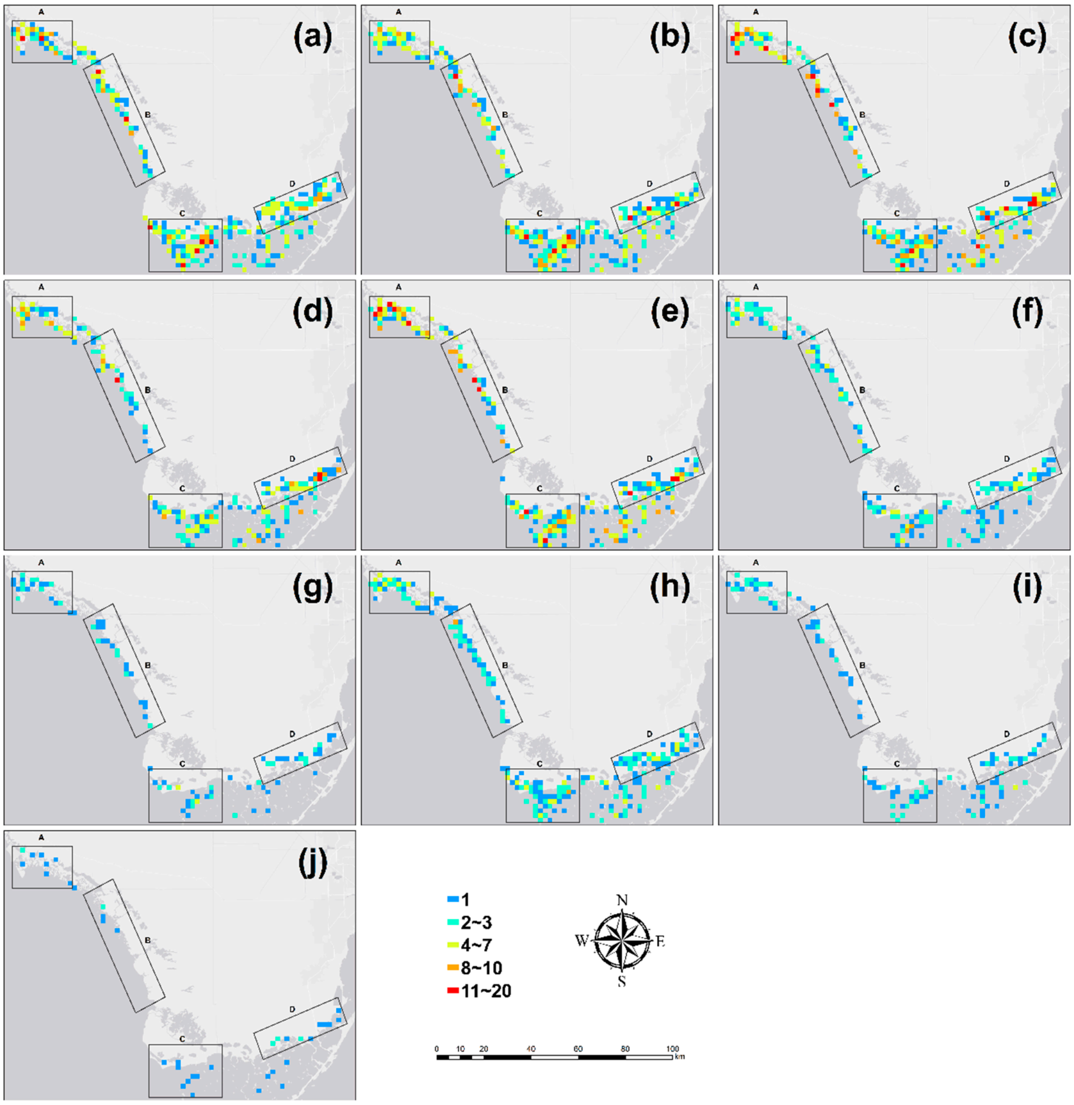

Figure 19. Spatial distributions of all types of events by occurrences per 4 km^2 grid: (**a**) appearance; (**b**) disappearance; (**c**) contraction; (**d**) stability; (**e**) expansion; (**f**) merger; (**g**) annexation; (**h**) splitting; (**i**) separation; and (**j**) recovery.

According to Section 3.3.1, the tidal flat cells are intensively distributed in four regions within the study area, which should potentially affect the spatial distribution of each event. This is proved with Figure 19, as all types of events are mainly distributed within or around the four regions. Accordingly, the occurrence places of these events are counted by five classes (the four intensive regions and the rest region), and the summary is drawn in Figure 20. This figure shows that 89.47% of *annexation* events and 75.44% of *separation* events are distributed within the four regions, which are the highest and lowest records among all types of events and verify the above finding. Another interesting finding is that even though the tidal flat area in region C is not the largest among the four regions, a total of eight types of events (*appearance*, *disappearance*, *contraction*, *expansion*, *merger*, *annexation*, *splitting*, and *separation*) are more in region C than elsewhere. Similarly, although the tidal flat area in region A is the smallest among the four regions, the number of event occurrences in region A is ranked as the third most among the four regions in cases of *appearance*, *disappearance*, and *stability* events and the second most among the four regions in cases of the rest event types. Therefore, we can conclude that the tidal flat dynamic activities are more frequent in regions A and C than regions B and D. This may be explained by regarding the fact that the tidal flat areas in regions B and D are mostly the products of the principal natural drainages, which are different from the cases of regions A and C.

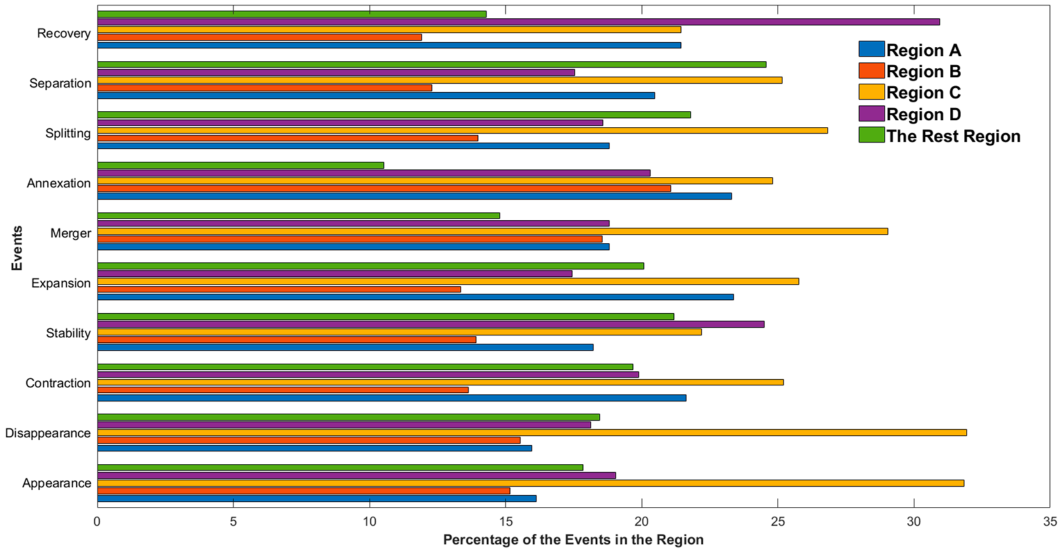

Figure 20. Percentage of all types of events by regions.

The above spatiotemporal characteristics for the events prove that the graph representation in our case study can visualize the tracked tidal flat lifecycles and make it possible to capture the events from them. In addition, the graph operators in our case study provide an effective way to automatically and exhaustively capture the events from a large amount of tidal flat lifecycles, which also highlights that the object and lifecycle levels could provide more diversified dynamic information than the cell level.

4. Conclusions

An integrated approach of three-level GIS framework and graph model is proposed in this study, which provides an effective way to track, represent, and analyze the dynamic activities of tidal flats from a novel perspective. The three-level GIS framework consists of the cell level, the object level, and the lifecycle level. Furthermore, a variety types of events are defined based on (1) the numbers of predecessors or successors of each tidal flat object; and (2) the area comparison between the predecessor and successor. These events provide an enhanced way to describe the dynamic activities of tidal flats throughout their lifecycles.

On the other hand, the graph model conceptualizes the tidal flat objects as the nodes, and the predecessor–successor relationships as the edges. As the derivative of the graph model, a spatiotemporal database is derived simultaneously, which offers the storage and query features for a variety types of morphologic attributes of tidal flats. In addition, graph operators are introduced in this study, which assist the proposed graph model to capture the events automatically and exhaustively.

In the case study, all GEE-archived Landsat imageries from 1984 to 2018 in the study area are invoked, and the RF machine learning algorithm is used to extract tidal flat cells from them. The tidal flat cells are assembled as tidal flat objects, which are further linked as tidal flat lifecycles with respect to the predecessor–successor relationships. The MATLAB prototype system is implemented to track, represent, and analyze the dynamic activities of tidal flats. The results imply that the geology, hydrology, and meteorology factors may affect the dynamic activities of tidal flats in the southwest tip of Florida Peninsula.

Our research is the first effort that systematically organizes the multi-level GIS framework and graph theory to track, represent, and analyze the dynamic activities of tidal flats, which also provides a novel perspective to examine the other dynamic geographic phenomena with large spatiotemporal scales. The future work will be conducted in three aspects. First, we plan to involve the whole coastal area of the conterminous US to implement this integrated approach, to not only verify its universality and robustness, but also find more diversified spatiotemporal regularities of tidal flat dynamic activities. Second, we are also interested in the in-depth explorations for the natural and anthropogenic factors, which may potentially affect the spatiotemporal characteristics of tidal flat dynamic activities such as urbanization and sea level rise. Third, we noticed that the NOAA tide stations (https://tidesandcurrents.noaa.gov/) are producing high temporal resolution data of the water level along the US coast, which enables and encourages us to contribute to the interdisciplinary research collaborated with the colleagues of coastal hydrology and oceanography backgrounds.

Author Contributions: Conceptualization, Weibo Liu; Methodology, Weibo Liu and Chao Xu; Software, Chao Xu; Formal Analysis, Chao Xu and Weibo Liu; Writing- Original Draft Preparation, Chao Xu and Weibo Liu; Writing-Review & Editing, Weibo Liu. All authors have read and agreed to the published version of the manuscript.

Funding: This research received no external funding.

Data Availability Statement: Publicly available datasets were analyzed in this study. This data can be found here: https://developers.google.com/earth-engine/datasets/.

Acknowledgments: We would like to thank the four anonymous reviewers and editors for providing valuable comments and suggestions which helped improve the manuscript greatly.

Conflicts of Interest: The authors declare no conflict of interest.

References

1. Worboys, M. Event-oriented approaches to geographic phenomena. *Int. J. Geogr. Inf. Sci.* **2005**, *19*, 1–28. [CrossRef]
2. Armstrong, M.P. Temporality in Spatial Databases. In Proceedings of the GIS/LIS'88, San Antonio, TX, USA, 30 November–2 December 1988; Volume 2, pp. 880–889.
3. Chrisman, N.R. Beyond the Snapshot: Changing the Approach to Change. In *Spatial and Temporal Reasoning in Geographic Information Systems*; Oxford University Press: Oxford, UK, 1998; p. 85.
4. Hornsby, K.; Egenhofer, M.J. Identity-based change: A foundation for spatio-temporal knowledge representation. *Int. J. Geogr. Inf. Sci.* **2000**, *14*, 207–224. [CrossRef]
5. Peuquet, D.J.; Duan, N. An event-based spatiotemporal data model (ESTDM) for temporal analysis of geographical data. *Int. J. Geogr. Inf. Syst.* **1995**, *9*, 7–24. [CrossRef]
6. Claramunt, C.; Thériault, M. Managing Time in GIS An Event-Oriented Approach. In *Recent Advances in Temporal Databases*; Springer: London, UK, 1995; pp. 23–42.
7. Yuan, M. Representing complex geographic phenomena in GIS. *Cartogr. Geogr. Inf. Sci.* **2001**, *28*, 83–96. [CrossRef]
8. Yuan, M.; Hornsby, K.S. *Computation and Visualization for Understanding Dynamics in Geographic Domains: A Research Agenda*; CRC Press: Boca Raton, FL, USA, 2007.
9. McIntosh, J.; Yuan, M. A framework to enhance semantic flexibility for analysis of distributed phenomena. *Int. J. Geogr. Inf. Sci.* **2005**, *19*, 999–1018. [CrossRef]
10. Thibaud, R.; del Mondo, G.; Garlan, T.; Mascret, A.; Carpentier, C. A spatio-temporal graph model for marine dune dynamics analysis and representation. *Trans. GIS* **2013**, *17*, 742–762. [CrossRef]
11. Yi, J.; Du, Y.; Liang, F.; Zhou, C.; Wu, D.; Mo, Y. A representation framework for studying spatiotemporal changes and interactions of dynamic geographic phenomena. *Int. J. Geogr. Inf. Sci.* **2014**, *28*, 1010–1027. [CrossRef]
12. Liu, W.; Li, X.; Rahn, D.A. Storm event representation and analysis based on a directed spatiotemporal graph model. *Int. J. Geogr. Inf. Sci.* **2016**, *30*, 948–969. [CrossRef]
13. Zhu, R.; Guilbert, E.; Wong, M.S. Object-oriented tracking of the dynamic behavior of urban heat islands. *Int. J. Geogr. Inf. Sci.* **2017**, *31*, 405–424. [CrossRef]
14. Wu, B.; Yu, B.; Shu, S.; Wu, Q.; Zhao, Y.; Wu, J. A spatiotemporal structural graph for characterizing land cover changes. *Int. J. Geogr. Inf. Sci.* **2020**, *35*, 1–29. [CrossRef]
15. Cheung, A.K.L.; O'sullivan, D.; Brierley, G. Graph-assisted landscape monitoring. *Int. J. Geogr. Inf. Sci.* **2015**, *29*, 580–605. [CrossRef]

16. Wu, Q.; Su, H.; Sherman, D.J.; Liu, H.; Wozencraft, J.M.; Yu, B.; Chen, Z. A graph-based approach for assessing storm-induced coastal changes. *Int. J. Remote Sens.* **2016**, *37*, 4854–4873. [CrossRef]
17. Britannica, E. *Encyclopædia Britannica*; Encyclopædia Britannica, Inc.: Chicago, IL, USA, 2006.
18. Chan, Y.C.; Peng, H.B.; Han, Y.X.; Chung, S.S.W.; Li, J.; Zhang, L.; Piersma, T. Conserving unprotected important coastal habitats in the Yellow Sea: Shorebird occurrence, distribution and food resources at Lianyungang. *Glob. Ecol. Conserv.* **2019**, *20*, e00724. [CrossRef]
19. Li, P.D.; Jeewon, R.; Aruna, B.; Li, H.Y.; Lin, F.C.; Wang, H.K. Metabarcoding reveals differences in fungal communities between unflooded versus tidal flat soil in coastal saline ecosystem. *Sci. Total Environ.* **2019**, *690*, 911–922. [CrossRef]
20. Saad, J.F.; Narvarte, M.A.; Abrameto, M.A.; Alder, V.A. Drivers of nano-and microplanktonic community structure in a Patagonian tidal flat ecosystem. *J. Plankton Res.* **2019**, *41*, 621–639. [CrossRef]
21. Kaneko, S.; Kanou, K.; Sano, M. Differences in fish assemblage structures between tidal marsh and bare sandy littoral habitats in a brackish water lake, eastern Japan. *Ichthyol. Res.* **2020**, *67*, 439–450. [CrossRef]
22. Rabenhorst, M.C. Carbon storage in tidal marsh soils. *Soils Glob. Chang.* **1995**, *5*, 93–103.
23. Chmura, G.L.; Anisfeld, S.C.; Cahoon, D.R.; Lynch, J.C. Global carbon sequestration in tidal, saline wetland soils. *Glob. Biogeochem. Cycles* **2003**, *17*, 1917. [CrossRef]
24. Klaassen, W.; Spilmont, N. Inter-annual variability of CO_2 exchanges between an emersed tidal flat and the atmosphere. *Estuar. Coast. Shelf Sci.* **2012**, *100*, 18–25. [CrossRef]
25. Liu, J.; Song, Z.; Wang, J.; Bouwman, A.F.; Li, M.; Liu, S.; Cao, L.; Zang, J.; Ran, X. Biogenic Silica Composition and Storage in the Yellow River Delta Wetland with Implications for the Carbon Preservation. *Wetlands* **2019**, *40*, 1085–1095. [CrossRef]
26. Tan, L.; Ge, Z.; Zhou, X.; Li, S.; Li, X.; Tang, J. Conversion of coastal wetlands, riparian wetlands, and peatlands increases greenhouse gas emissions: A global meta-analysis. *Glob. Chang. Biol.* **2020**, *26*, 1638–1653. [CrossRef] [PubMed]
27. Davidson, N.C.; Van Dam, A.A.; Finlayson, C.M.; McInnes, R.J. Worth of wetlands: Revised global monetary values of coastal and inland wetland ecosystem services. *Mar. Freshw. Res.* **2019**, *70*, 1189–1194. [CrossRef]
28. Zhang, K.; Dong, X.; Liu, Z.; Gao, W.; Hu, Z.; Wu, G. Mapping Tidal Flats with Landsat 8 Images and Google Earth Engine: A Case Study of the China's Eastern Coastal Zone circa 2015. *Remote Sens.* **2019**, *11*, 924. [CrossRef]
29. Wang, X.; Xiao, X.; Zou, Z.; Chen, B.; Ma, J.; Dong, J.; Doughty, R.B.; Zhong, Q.; Qin, Y.; Dai, S.; et al. Tracking annual changes of coastal tidal flats in China during 1986–2016 through analyses of Landsat images with Google Earth Engine. *Remote Sens. Environ.* **2020**, *238*, 110987. [CrossRef]
30. Taylor, R.B.; Sagar, S.; Lymburner, L.; Beaman, R.J. Between the tides: Modelling the elevation of Australia's exposed intertidal zone at continental scale. *Estuar. Coast. Shelf Sci.* **2019**, *223*, 115–128. [CrossRef]
31. Murray, N.J.; Phinn, S.R.; de Witt, M.; Ferrari, R.; Johnston, R.; Lyons, M.B.; Clinton, N.; Thau, D.; Fuller, R.A. The global distribution and trajectory of tidal flats. *Nature* **2019**, *565*, 222. [CrossRef]
32. McFeeters, S.K. The use of the Normalized Difference Water Index (NDWI) in the delineation of open water features. *Int. J. Remote Sens.* **1996**, *17*, 1425–1432. [CrossRef]
33. Xiao, X.; Hollinger, D.; Aber, J.; Goltz, M.; Davidson, E.A.; Zhang, Q.; Moore, B., III. Satellite-based modeling of gross primary production in an evergreen needleleaf forest. *Remote Sens. Environ.* **2004**, *89*, 519–534. [CrossRef]
34. Xu, H. Modification of normalised difference water index (NDWI) to enhance open water features in remotely sensed imagery. *Int. J. Remote Sens.* **2006**, *27*, 3025–3033. [CrossRef]
35. Feyisa, G.L.; Meilby, H.; Fensholt, R.; Proud, S.R. Automated Water Extraction Index: A new technique for surface water mapping using Landsat imagery. *Remote Sens. Environ.* **2014**, *140*, 23–35. [CrossRef]
36. Sousa, W.R.D.; Souto, M.V.; Matos, S.S.; Duarte, C.R.; Salgueiro, A.R.; Neto, C.A.D.S. Creation of a coastal evolution prognostic model using shoreline historical data and techniques of digital image processing in a GIS environment for generating future scenarios. *Int. J. Remote Sens.* **2018**, *39*, 4416–4430. [CrossRef]
37. Li, W.; Gong, P. Continuous monitoring of coastline dynamics in western Florida with a 30-year time series of Landsat imagery. *Remote Sens. Environ.* **2016**, *179*, 196–209. [CrossRef]
38. Liu, Y.; Wang, X.; Ling, F.; Xu, S.; Wang, C. Analysis of coastline extraction from Landsat-8 OLI imagery. *Water* **2017**, *9*, 816. [CrossRef]
39. Wang, X.; Liu, Y.; Ling, F.; Liu, Y.; Fang, F. Spatio-Temporal change detection of Ningbo coastline using Landsat time-series images during 1976–2015. *ISPRS Int. J. Geo Inf.* **2017**, *6*, 68. [CrossRef]
40. Xu, N. Detecting coastline change with all available landsat data over 1986–2015: A case study for the state of Texas, USA. *Atmosphere* **2018**, *9*, 107. [CrossRef]
41. Xu, N.; Jia, D.; Ding, L.; Wu, Y. Continuously Tracking the Annual Changes of the Hengsha and Changxing Islands at the Yangtze River Estuary from 1987 to 2016 Using Landsat Imagery. *Water* **2018**, *10*, 171. [CrossRef]
42. Lin, Y.; Cai, Y.; Gong, Y.; Kang, M.; Li, L. Extracting urban landmarks from geographical datasets using a random forests classifier. *Int. J. Geogr. Inf. Sci.* **2019**, *33*, 2406–2423. [CrossRef]
43. Teluguntla, P.; Thenkabail, P.S.; Oliphant, A.; Xiong, J.; Gumma, M.K.; Congalton, R.G.; Yadav, K.; Huete, A. A 30-m landsat-derived cropland extent product of Australia and China using random forest machine learning algorithm on Google Earth Engine cloud computing platform. *ISPRS J. Photogramm. Remote Sens.* **2018**, *144*, 325–340. [CrossRef]

44. Oliphant, A.J.; Thenkabail, P.S.; Teluguntla, P.; Xiong, J.; Gumma, M.K.; Congalton, R.G.; Yadav, K. Mapping cropland extent of Southeast and Northeast Asia using multi-year time-series Landsat 30-m data using a random forest classifier on the Google Earth Engine Cloud. *Int. J. Appl. Earth Obs. Geoinf.* **2019**, *81*, 110–124. [CrossRef]
45. Johansen, K.; Phinn, S.; Taylor, M. Mapping woody vegetation clearing in Queensland, Australia from Landsat imagery using the Google Earth Engine. *Remote Sens. Appl. Soc. Environ.* **2015**, *1*, 36–49. [CrossRef]
46. Patel, N.N.; Angiuli, E.; Gamba, P.; Gaughan, A.; Lisini, G.; Stevens, F.R.; Tatem, A.J.; Trianni, G. Multitemporal settlement and population mapping from Landsat using Google Earth Engine. *Int. J. Appl. Earth Obs. Geoinf.* **2015**, *35*, 199–208. [CrossRef]
47. Goldblatt, R.; You, W.; Hanson, G.; Khandelwal, A.K. Detecting the boundaries of urban areas in india: A dataset for pixel-based image classification in google earth engine. *Remote Sens.* **2016**, *8*, 634. [CrossRef]
48. Medeiros, S.C.; Hagen, S.C.; Weishampel, J.F. A Random Forest model based on lidar and field measurements for parameterizing surface roughness in coastal modeling. *IEEE J. Sel. Top. Appl. Earth Obs. Remote Sens.* **2015**, *8*, 1582–1590. [CrossRef]
49. Pettorelli, N.; Vik, J.O.; Mysterud, A.; Gaillard, J.M.; Tucker, C.J.; Stenseth, N.C. Using the satellite-derived NDVI to assess ecological responses to environmental change. *Trends Ecol. Evol.* **2005**, *20*, 503–510. [CrossRef]
50. Huete, A.; Didan, K.; Miura, T.; Rodriguez, E.P.; Gao, X.; Ferreira, L.G. Overview of the radiometric and biophysical performance of the MODIS vegetation indices. *Remote Sens. Environ.* **2002**, *83*, 195–213. [CrossRef]
51. Qi, J.; Chehbouni, A.; Huete, A.R.; Kerr, Y.H.; Sorooshian, S. A modified soil adjusted vegetation index. *Remote Sens. Environ.* **1994**, *48*, 119–126. [CrossRef]
52. Baig, M.H.A.; Zhang, L.; Shuai, T.; Tong, Q. Derivation of a tasselled cap transformation based on Landsat 8 at-satellite reflectance. *Remote Sens. Lett.* **2014**, *5*, 423–431. [CrossRef]
53. Amante, C.; Eakins, B.W. ETOPO1 1 Arc-minute global relief model: Procedures, data sources and analysis. NOAA Technical Memorandum NESDIS NGDC-24. *Natl. Geophys. Data Cent. NOAA* **2009**, *10*, V5C8276M.
54. Pekel, J.F.; Cottam, A.; Gorelick, N.; Belward, A.S. High-resolution mapping of global surface water and its long-term changes. *Nature* **2016**, *540*, 418–422. [CrossRef]
55. Rosenfeld, A. *Digital Picture Processing*; Academic Press: Cambridge, MA, USA, 1976.
56. Haralick, R.M.; Shapiro, L.G. *Computer and Robot. Vision*; Addison-Wesley: Boston, MA, USA, 1992; Volume 1, pp. 28–48.
57. Wilson, R.J. *Introduction to Graph Theory*, 4th ed.; Longman Group Ltd.: Essex, UK, 1996.
58. Gorelick, N.; Hancher, M.; Dixon, M.; Ilyushchenko, S.; Thau, D.; Moore, R. Google Earth Engine: Planetary-scale geospatial analysis for everyone. *Remote Sens. Environ.* **2017**, *202*, 18–27. [CrossRef]
59. Solecki, W.D.; Long, J.; Harwell, C.C.; Myers, V.; Zubrow, E.; Ankersen, T.; Deren, C.; Feanny, C.; Hamann, R.; Hornung, L.; et al. Human-environment interactions in South Florida's Everglades region: Systems of ecological degradation and restoration. *Urban. Ecosyst.* **1999**, *3*, 305–343. [CrossRef]
60. Petuch, E.J.; Roberts, C. *The Geology of the Everglades and Adjacent Areas*; CRC Press: Boca Raton, FL, USA, 2007.
61. Richardson, C.J. The everglades: North America's subtropical wetland. *Wetl. Ecol. Manag.* **2010**, *18*, 517–542. [CrossRef]
62. Smoak, J.M.; Breithaupt, J.L.; Smith, T.J., III; Sanders, C.J. Sediment accretion and organic carbon burial relative to sea-level rise and storm events in two mangrove forests in Everglades National Park. *Catena* **2013**, *104*, 58–66. [CrossRef]
63. Zhu, Z.; Woodcock, C.E. Object-based cloud and cloud shadow detection in Landsat imagery. *Remote Sens. Environ.* **2012**, *118*, 83–94. [CrossRef]
64. Zhu, Z.; Wang, S.; Woodcock, C.E. Improvement and expansion of the Fmask algorithm: Cloud, cloud shadow, and snow detection for Landsats 4–7, 8, and Sentinel 2 images. *Remote Sens. Environ.* **2015**, *159*, 269–277. [CrossRef]
65. Risi, J.A.; Wanless, H.R.; Tedesco, L.P.; Gelsanliter, S. Catastrophic sedimentation from Hurricane Andrew along the southwest Florida coast. *J. Coast. Res.* **1995**, 83–102.
66. Lou, S.; Huang, W.; Liu, S.; Zhong, G.; Johnson, E. Hurricane impacts on turbidity and sediment in the Rookery Bay National Estuarine Research Reserve, Florida, USA. *Int. J. Sediment. Res.* **2016**, *31*, 330–340. [CrossRef]
67. Gebelein, C.D. *Dynamics of Recent Carbonate Sedimentation and Ecology, Cape Sable, Florida*; Brill: Leiden, Netherlands, 1977; Volume 16.
68. Franklin, J.L.; Pasch, R.J.; Avila, L.A.; Beven, J.L.; Lawrence, M.B.; Stewart, S.R.; Blake, E.S. Atlantic hurricane season of 2004. *Mon. Weather Rev.* **2006**, *134*, 981–1025. [CrossRef]